Comprehensive model of damage accumulation in silicon

K. R. C. Mok,[1,a)] F. Benistant,[1] M. Jaraiz,[2] J. E. Rubio,[2] P. Castrillo,[2] R. Pinacho,[2] and M. P. Srinivasan[3]

[1]*Chartered Semiconductor Manufacturing, 60 Woodlands, Industrial Park D, Street 2, Singapore 738406, Singapore*

[2]*Departamento de E. y Electrónica, Universidad de Valladolid, ETSIT Campus Miguel Delibes, 47011 Valladolid, Spain*

[3]*Department of Chemical & Biomolecular Engineering, National University of Singapore, 4 Engineering Drive 4, Singapore 117576, Singapore*

(Received 16 March 2007; accepted 9 November 2007; published online 15 January 2008)

Ion implantation induced damage accumulation is crucial to the simulation of silicon processing. We present a physically based damage accumulation model, implemented in a nonlattice atomistic kinetic Monte Carlo simulator, that can simulate a diverse range of interesting experimental observations. The model is able to reproduce the ion-mass dependent silicon amorphous-crystalline transition temperature of a range of ions from C to Xe, the amorphous layer thickness for a range of amorphizing implants, the superlinear increase in damage accumulation with dose, and the two-layered damage distribution observed along the path of a high-energy ion. In addition, this model is able to distinguish between dynamic annealing and post-cryogenic implantation annealing, whereby dynamic annealing is more effective in removing damage than post-cryogenic implantation annealing at the same temperature. © *2008 American Institute of Physics*.
[DOI: 10.1063/1.2829815]

I. INTRODUCTION

Ion implantation processing is a field of considerable scientific and technological interest, as it is a standard process in the fabrication of integrated circuits, for purposes such as the controlled doping of silicon and for preamorphization implants.[1] In crystalline semiconductor materials, understanding and modeling of the ion implantation induced damage accumulation is crucial to the simulation of silicon processing. For example, it is important to predict the position of the amorphous-crystalline interface as it impacts damage evolution during the subsequent annealing step, with significant consequences on dopant diffusion and activation.[2]

However, modeling of damage accumulation is difficult due to the complex variety of damage induced by ion implantation and the many interdependent implantation parameters, such as ion mass,[3,4] dose,[5,6] dose rate,[3,7,8] and substrate temperature.[3,8] A single accurate model should be capable of properly accounting for experimental observations, taking into account ion mass effects and the dynamic annealing process that results in the experimentally observed dose rate and substrate temperature effects. In addition, the model should be implemented in a manner efficient for practical device-sized process simulations.

Damage accumulation due to subsequent implantation cascades is a competition between damage generation and dynamic annealing. Both mechanisms are dependent on implantation parameters. An increase in dose rate increases the rate of damage generation, while an increase in substrate temperature increases the rate of annihilation of defects, thereby reducing the effective rate of damage accumulation.[9]

In trying to understand the complex mechanism of damage accumulation, various experimental[10] and theoretical works[11] have pointed to a continuous range of activation energies for the recrystallization of the highly disordered damage pockets induced by the ion implantation process. Molecular dynamics (MD) study of implantation cascades in silicon shows that a single ion can result in the production of amorphous pockets, as well as isolated point defects and small clusters, with only interstitial (I) or vacancy (V) defects.[11] The resulting damage can vary in configuration, size, and shape, with a strong dependence on ion mass. Further recrystallization of the amorphous pockets by annealing shows that larger pockets have larger effective activation energy of recrystallization, indicating greater stability against recrystallization. Moreover, MD simulations based on a bond defect, also known as an IV pair, have shown that IV pairs that are isolated or scattered recombine very quickly, but, in high concentration, the IV pairs can interact to form more stable structures that accumulate, giving rise to amorphization.[12] Experimental studies also show a consistent understanding of damage accumulation. The apparent activation energies for the amorphous-crystalline phase transition for C (12 u) to Xe (132 u) have been determined to range from 0.7 eV (for C) to 1.7 eV (for Xe), increasing with ion mass[3] (see Fig. 1). Nanocalorimetry experiments also suggest that the continuous rate of heat release can be explained by the annealing of a collection of highly disordered pockets.[10]

We have already presented a damage accumulation model that can reproduce the silicon amorphous-crystalline transition temperature for C, Si, and Ge ion implants.[13] In short, the model is implemented in a nonlattice atomistic kinetic Monte Carlo simulator[14] and is based on ion-implant damage structures known as the amorphous pockets (I_nV_m),

a)Electronic mail: carolinemok@charteredsemi.com.

 © 2008 American Institute of Physics

Downloaded 21 Apr 2008 to 157.88.111.70. Redistribution subject to AIP license or copyright; see http://jap.aip.org/jap/copyright.jsp

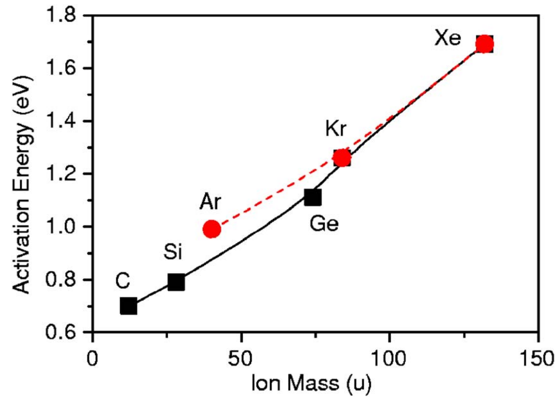

FIG. 1. (Color online) Activation energy of recrystallization as a function of implant ion mass from experimental data of Ref. 3. (Lines drawn to guide the eyes.)

whereby the amorphous pocket recrystallization rate (shrinkage rate) is characterized by the effective size of the amorphous pockets, $s=\min(n,m)$. In this model, damage can nucleate from isolated IV pairs, I_2 and V_2, resulting in more complex amorphous pockets, I_nV_m, and further building up to amorphization. The self-consistent treatment of pure I, V clusters, and amorphous pockets I_nV_m allows for the model to account for the contribution of damage from point defects, amorphous pockets, and pure clusters.

In this work, we extend the capability of the model to reproduce the amorphous-crystalline transition temperatures from C to Xe and show that the model can provide accurate prediction of the amophous layer thickness and is able to simulate results consistent with experimental observations of dose and temperature effects.

II. MODEL

One of the initial tasks in modeling amorphization is to establish the amorphization threshold. Values of the amorphization threshold obtained from the literature vary widely from 5% to 50% of the atomic density of silicon, with no systematic dependence on ion species or implant energy (see Ref. 15 and references therein).

The accumulation of amorphous pockets is assumed to give rise to locally, fully amorphized regions where the defect concentration (I+V) reaches the amorphization threshold. Due to dynamic annealing, the critical minimum dose for amorphization is a strong function of implant temperature. For a given ion, the critical amorphization dose increases with implant temperature. Hence, the amorphization threshold used in the model has to be determined from low temperature (100 K) implantation experiments,[16] whereby dynamic annealing can be assumed to be negligible.

Based on experiments, the critical amorphization doses required to produce a continuous amorphous layer for 200 keV B and P and 300 keV Sb implanted at 100 K and 1.25×10^{12} cm^{-2} s^{-1} are 1×10^{15} cm^{-2}, 2×10^{14} cm^{-2} and 3×10^{13} cm^{-2} respectively. The critical dose for amorphization for all three ions can be accurately simulated using an amorphization threshold of 1.5×10^{22} defects (I+V) cm^{-3}.

Figure 2(a) shows a continuous, buried amorphous layer formed by 200 keV B implanted at 100 K and 1.25×10^{12} cm^{-2} s^{-1} up to the critical dose of 1×10^{15} cm^{-2}, while Fig. 2(b) shows highly damaged but still non-amorphized silicon substrate resulting from implantation up to half the critical dose. Notice that the same amorphization threshold is able to reproduce the critical amorphization doses for implant ions of different masses, from light B to heavy Sb ions.

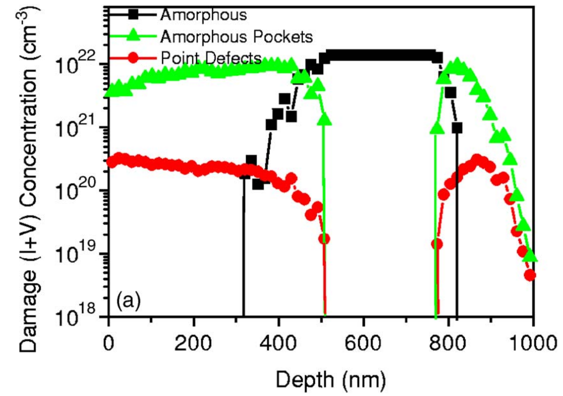

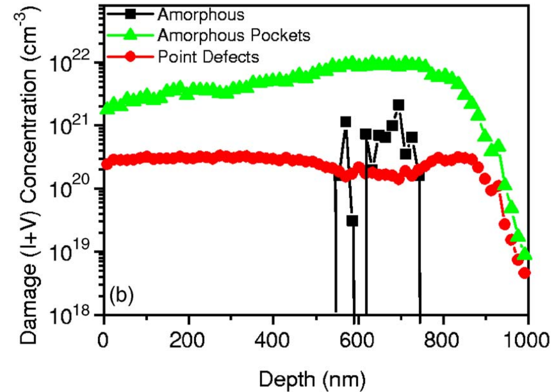

FIG. 2. (Color online) Simulated damage (total I+V) profiles for 200 keV B implant at 100 K and 1.25×10^{12} cm^{-2} s^{-1}. (a) Up to the critical dose of 1×10^{15} cm^{-2}. (b) Up to a dose of 5×10^{14} cm^{-2}.

In this model, an amorphous pocket (AP) of size s is assumed to shrink to $(s-1)$ at a rate given by $\alpha s^{\beta}\exp[-E_{\text{act}}(s)/kT]$. The experimental data from Ref. 3 are used to determine the model parameters. The experimental data correspond to the amorphous-crystalline transition temperatures, as a function of dose rate, for (100) Si implanted with 80 keV ions to a dose of 1×10^{15} cm^{-2} for Si, Ar, Ge, Kr, and Xe, and 2×10^{15} cm^{-2} for C. In the simulations, the transition temperatures were determined as the maximum temperature that results in a buried continuous amorphous layer, as is consistent with the experimental procedure. The single set of parameters used is $\alpha=3\times10^{-4}$ cm^{-2}, $\beta=1.0$, and recrystallization activation energy as a function of size, as shown in Fig. 3. The maximum recrystallization activation energy is taken to be 2.7 eV, which is equal to that of a planar amorphous-crystalline interface of a fully amorphized region.[17] Although it was possible to fit one type of ion with different activation energy functions by varying the appropriate prefactor, the constraints imposed by the wide range of ion masses used in the calibration left practically no room for arbitrary assignments. Namely, with other activation energy assignments, there was insufficient temperature discrimination at either the high or low ion mass ends.

Downloaded 21 Apr 2008 to 157.88.111.70. Redistribution subject to AIP license or copyright; see http://jap.aip.org/jap/copyright.jsp

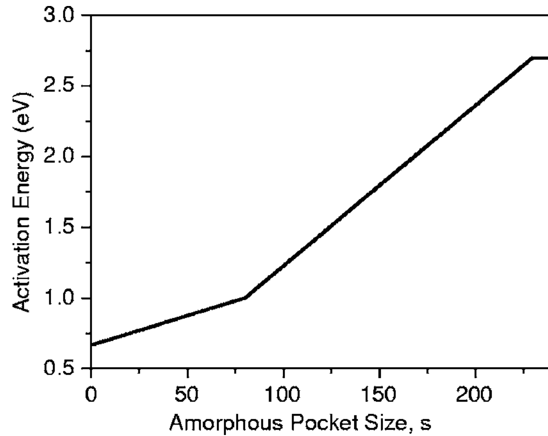

FIG. 3. Activation energy of recrystallization as a function of size of the amorphous pockets.

Figure 4 shows the best fit lines obtained from simulations of each ion. The model is able to very accurately reproduce all the experimental data for different ion masses, dose rates, and implant temperatures. In the case of noble gas implant simulations, the amorphization threshold was found to be lower than expected, and we interpret this peculiar behavior in terms of the lattice weakening effect of these non-bonding atoms. Although Ar has an ion mass between Si and Ge, its simulated transition temperature using the same activation energy function (as shown in Fig. 3) was lower than the experimental value. The dashed line in Fig. 4 represents the simulated amorphous-crystalline transition temperature for Ar using the standard procedure. This means that Ar amorphizes Si more easily than expected based on ion mass effect alone. This conjecture was clearly confirmed (see Fig. 1) when we plot the experimental activation energies from Ref. 3 as a function of ion mass. We attribute this additional effect to the non-bonding character of noble gas atoms, compared to the group IV elements. The presence of these non-bonding atoms weakens the silicon lattice locally and, in consequence, the lattice collapses to the amorphous state before the regular amorphization threshold is reached. This silicon lattice weakening effect by noble gas atoms has been verified by MD studies on silicon sputtering yield with Ar ions.[18]

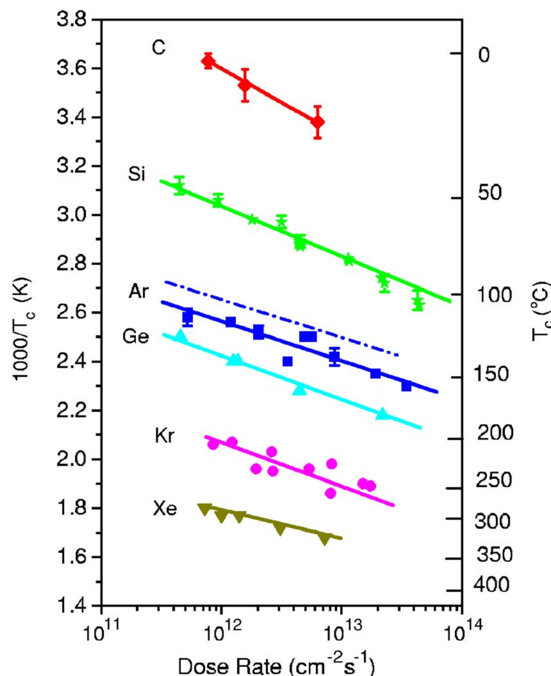

FIG. 4. (Color online) Simulation (lines) compared to experimental data (symbols) from Ref. 3 for amorphous-crystalline transition temperatures as a function of dose rate, for (100) silicon irradiated with 80 keV ions to a dose of 1×10^{15} cm^{-2} for Si, Ar, Ge, Kr, and Xe, and 2×10^{15} cm^{-2} for C. Solid lines for noble gases obtained by taking into account the lattice weakening effect of the noble gas atoms. Dashed line represents the transition temperatures for Ar using the standard procedure.

Assuming a linear dependence with non-bonding atom concentration, we assign a certain "already amorphized" volume (V_{am}=1.5 nm^3) to each implanted noble gas ion, so that they can effectively lower the amount of cascade-generated damage necessary to reach the amorphization threshold. As a first approximation, the same V_{am} volume was assumed for Ar, Kr, and Xe. Although the number of implanted noble gas ions (as well as V_{am}) is the same in all cases (same dose), both the experimental data (see Fig. 1) and our simulations suggest that this chemical (non-bonding atoms) effect becomes negligible for heavy noble gas ions. This can be understood by the fact that the transition temperature (and the corresponding activation energy) is such that the excess damage is annealed out. For a light noble gas ion like Ar, V_{am} is comparable to this excess damage per cascade, but it is negligible compared to the excess damage of a heavy ion cascade. Therefore, there is almost no difference in the temperature and activation energy needed to anneal out the excess damage for a heavy ion whether it is a noble gas (non-bonding atom) or not. We have also verified that the model predicts the saturation of the amorphous fraction for an 80 keV Ne (20 u) implant at a dose of 1×10^{15} cm^{-2}, in agreement with room temperature experimental data.[19]

III. RESULTS AND DISCUSSION

The amorphous-crystalline transition can be understood as the critical balance between damage generation and dynamic annealing. For a given implant condition, amorphization is not possible above the critical amorphous-crystalline transition temperature. For Si, this critical amorphous-crystalline transition temperature is close to room temperature.[3,7] Therefore, in this temperature range, the annealing time as determined by the dose rate will have a significant influence on the damage, which could range from minimally defected to fully amorphized. As dose rate increases, the time between the arrival of overlapping cascades decreases, reducing the rate of dynamic annealing, thereby resulting in increased damage accumulation. The nucleation of a buried, continuous amorphous layer and, ultimately, its thickness depend on the dose rate and substrate temperature, especially under conditions where dynamic defect annealing is significant.

A. Amorphous layer thickness

Figure 5 shows a sequence of simulations illustrating the development of the amorphous layer in Si with increasing

Downloaded 21 Apr 2008 to 157.88.111.70. Redistribution subject to AIP license or copyright; see http://jap.aip.org/jap/copyright.jsp

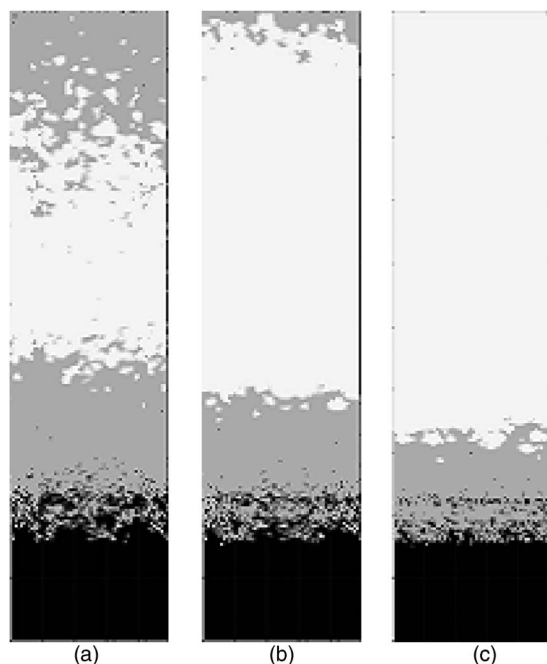

FIG. 5. Sequence of simulations showing the development of the amorphous layer in silicon with increasing dose of 300 keV Si: (a) 1×10^{15} cm^{-2}, (b) 2×10^{15} cm^{-2}, and (c) 5×10^{15} cm^{-2} implanted at 300 K with a dose rate of 1.5×10^{12} cm^{-2} s^{-1}. White represents amorphous regions and gray represents amorphous pockets. Simulation: 200×1000 nm^2.

dose of Si implanted at 300 keV, 300 K, and a dose rate of 1.5×10^{12} cm^{-2} s^{-1}, following the experimental conditions in Ref. 20.

The simulations are comparable with experimental cross-sectional transmission electron microscopy (TEM) micrographs shown in Ref. 20. At a dose of 1×10^{15} cm^{-2}, a buried amorphous layer is formed. The amorphous layer increases in thickness with increasing dose, reaching the surface at a dose of 5×10^{15} cm^{-2}.

In addition, the morphology of the amorphous-crystalline interface is also well-represented in the simulations. Due to damage straggling and dynamic annealing, a transition zone containing both amorphous and crystalline material exists, instead of an absolutely planar interface. Experimentally, the width of the transition zone has been observed to decrease with increasing amorphous layer thickness.[20] This is also reproduced by the simulations shown in Fig. 5.

From a practical, technological point of view, accurate prediction of the depth of the amorphous layer is important, especially for Ge preamorphization implant (PAI). This is because the formation of *p*-type ultra-shallow junction is often preceded by a Ge PAI step. This limits channeling of the subsequent low-energy B, so that the as-implanted B profile is shallower and more abrupt. The main drawback of this approach is the presence of residual defects in the end-of-range (EOR) region, just beyond the original amorphous-crystalline interface.[21] As the number of the interstitials stored in the EOR after recrystallization critically depends on the position of the amorphous-crystalline interface,[22] accurate simulation of the amorphous layer thickness is crucial as it impacts damage evolution during the subsequent annealing step.

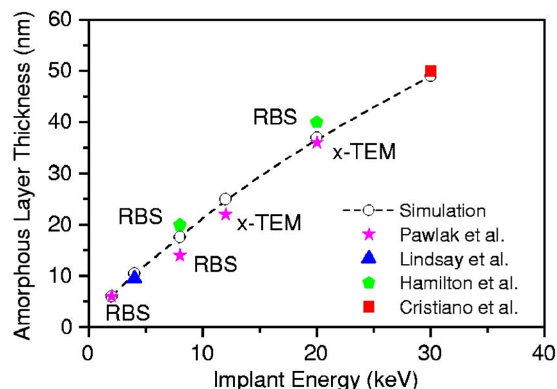

FIG. 6. (Color online) Amorphous layer thickness as a function of implant energy for Ge PAI at a dose of 1×10^{15} cm^{-2}. Simulations were done at room temperature and a dose rate of 1×10^{13} cm^{-2} s^{-1}. Filled symbols represent experimental data (Refs. 23–26), open symbols are from simulations. Experimental characterization methods are indicated when specified.

Figure 6 shows the amorphous layer thickness for a range of Ge PAI conditions. Ge is implanted up to a dose of 1×10^{15} cm^{-2} in all cases, for a range of energy from 2 to 30 keV. Since temperature and dose rate are not specified from the various references,[23–26] room temperature and a dose rate of 1×10^{13} cm^{-2} s^{-1} were used in all the simulations. When specified, the experimental characterization methods by Rutherford backscattering spectrometry (RBS) or cross-sectional transmission electron microscopy (x-TEM) are indicated in Fig. 6. As the amorphous-crystalline transition temperature for 80 keV, 1×10^{15} cm^{-2} Ge implant is much higher than room temperature,[3] it can be deduced that damage accumulation and amorphization for Ge implantation for the simulated conditions were not very sensitive to dose rate and temperature effects. A test was done for 20 keV Ge implant simulation. By varying the dose rate over an order of magnitude ($10^{12}-10^{14}$ cm^{-2} s^{-1}), the change in amorphous layer thickness is about ±3 nm, or less than 10%.

Figure 7 shows the amorphous layer thickness resulting from Ge PAI as a function of dose. Here 150 keV Ge was implanted to doses ranging from 1×10^{15} to 8×10^{15} cm^{-2}. As temperature and dose rate were not specified in the experimental procedure,[27] room temperature and a dose rate of 1×10^{13} cm^{-2} s^{-1} were again assumed for the simulations.

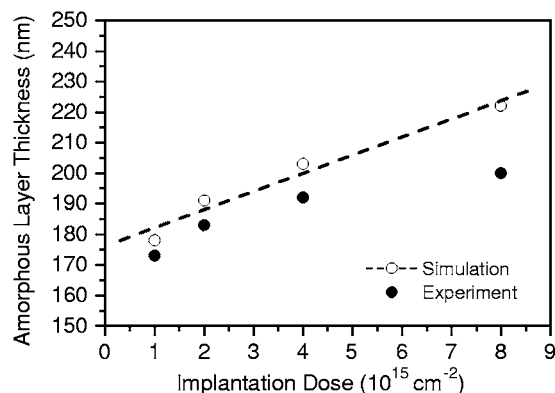

FIG. 7. Amorphous layer thickness as a function of dose for 150 keV Ge PAI. Simulations were done at room temperature and at a dose rate of 1×10^{13} cm^{-2} s^{-1}. Filled symbols represent experimental data measured by TEM (Ref. 27), open symbols are from simulations.

Downloaded 21 Apr 2008 to 157.88.111.70. Redistribution subject to AIP license or copyright; see http://jap.aip.org/jap/copyright.jsp

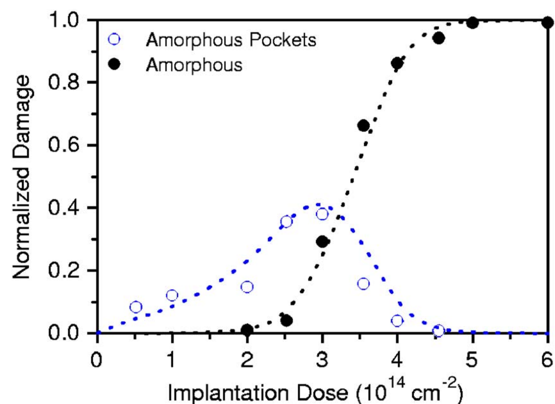

FIG. 8. (Color online) Dose dependence of damage produced by 100 keV Si ions at room temperature and a dose rate of 5×10^{12} cm^{-2} s^{-1}. Symbols show different damage components determined from the experimental annealing results from Ref. 5; dotted lines are results obtained from simulations.

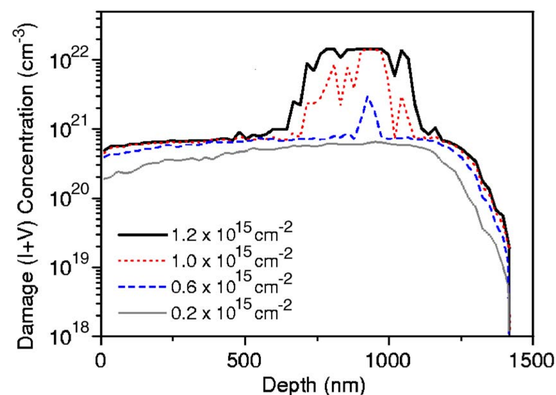

FIG. 9. (Color online) Simulated damage profile resulting from 1 MeV Si implantation at room temperature at various doses.

The discrepancy of between 3% and 11% between the simulated and experimental amorphous layer thickness may be attributed to the unspecified conditions of temperature and dose rate. However, it should be noted that this discrepancy increases with increase in dose. This can be expected as an increase in dose is likely to result in increased beam heating[28] and thereby increase in dynamic annealing.

B. Dose effect

Figure 8 shows the experimental[5] and simulated results for damage accumulation as a function of dose for 100 keV Si implant at room temperature. A dose rate of 5×10^{12} cm^{-2} s^{-1} was used in the simulations, consistent with the experimental procedure, which states that less than 1.2×10^{13} cm^{-2} s^{-1} was used.

Initially, damage from low dose implantation increases slowly with dose, until a critical dose (2×10^{14} cm^{-2}) is reached. This is because the damage (amorphous pockets) generated is relatively dilute and is not stable enough, therefore it is easily recrystallized by dynamic annealing. Subsequently, damage increases sharply within a narrow dose range, as the amorphous pockets become more stable, such that the rate of dynamic annealing is less than the rate of damage generation, resulting in effective damage accumulation. Finally, damage saturates as amorphization is reached, and further implantation only widens the amorphous layer.

An interesting feature that can be observed from Fig. 8 is the nature of the defect structures. Two different types of defect structures can be distinguished from simulations. They are, namely, the amorphous pockets and amorphous regions, which show different dose dependence. Initially, the dominant damage is the amorphous pocket. As the amorphous pockets increase in concentration, localized amorphous regions nucleate at a certain point (dose $\approx2\times10^{14}$ cm^{-2}). After the nucleation of localized amorphized regions, the amorphous damage becomes increasingly more dominant at the expense of the amorphous pockets. From Fig. 8, it can be seen that the proportion of the defect types from simulation is remarkably consistent with experimental observations by Holland *et al.*,[5] whereby the amorphous pockets (I_nV_m) in this model are actually the defects identified as divacancies in theirs. According to the authors, the divacancy-type defects are considered to be defect types that anneal around 250 °C.

Another experimental observation that can be reproduced by this model is the damage distribution with increasing dose. Under certain implant conditions, two distinct damage layers may be observed in silicon samples by RBS.[29,30] For example, for the damage accumulation in silicon induced by high energy (1.25 MeV) Si implant at room temperature, damage increases with dose up to amorphization near the EOR, while in the near surface region, damage saturates at a low level.[30]

Holland *et al.*[30] suggested that the near surface low level damage saturation could be explained by a homogeneous nucleation and growth damage accumulation model, whereby a dynamic balance exists between the various defect reactions considered relevant at room temperature. The various simple defect reactions include interstitial-vacancy recombination, defect clustering forming I_2 and V_2, and cluster recombination through point defect capture. The high damage region near the EOR was attributed to the imbalance in interstitials and vacancies, due to additional atoms during implantation and the spatial separation of Frenkel pairs created during ion impact. As a result, amorphous Si nucleates, further upsetting the balance between the simple defect reactions, eventually leading to amorphization.

Figure 9 shows the simulated damage profile resulting from a high energy (1 MeV) Si implantation at room temperature at various doses. Based on this damage accumulation model, the two distinct damage layers were clearly reproduced. At a depth of around 1 μm, damage increases with dose until amorphization occurs at a dose of 1×10^{15} cm^{-2}. At this depth, damage accumulates slowly up to a dose of 4×10^{14} cm^{-2}. Beyond 4×10^{14} cm^{-2}, there is a sudden growth of damage accumulation up to amorphization. This is in contrast with the near surface region, where damage accumulation increases slowly with dose up to 6×10^{14} cm^{-2} and subsequently saturates at a level regardless of the increase in implantation dose. Once a buried amorphous layer is nucleated, subsequent implantation would cause it to expand and extend toward the near surface region.

Downloaded 21 Apr 2008 to 157.88.111.70. Redistribution subject to AIP license or copyright; see http://jap.aip.org/jap/copyright.jsp

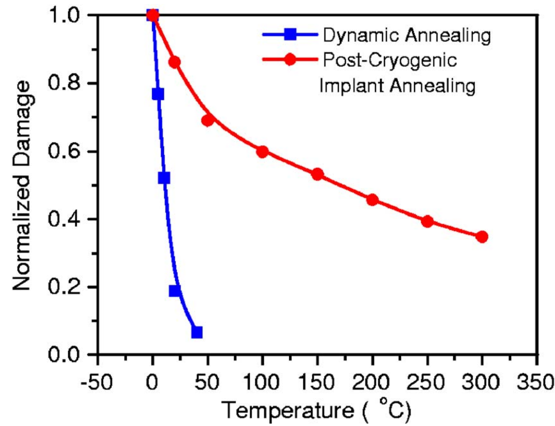

FIG. 10. (Color online) Simulated normalized damage as a function of temperature for 80 keV C implantations. Post-cryogenic implantation annealing represents 10 min annealing after cryogenic temperature (−150 °C) implantation.

C. Temperature effect

As mentioned, temperature has a significant effect on damage accumulation, such that the critical dose of amorphization is a strong function of the implant temperature. Besides the temperature dependence on implantation damage, another temperature effect that had been studied was the difference between dynamic annealing during the implantation and the post-implant annealing of cryogenic temperature implantation. Westmoreland *et al.*[31] had shown that the anneal behavior of the damage created in Si by 200 keV B ions is a strong function of temperature. More importantly, it was found that dynamic annealing during implantation was more effective than annealing at the same temperature following a cryogenic temperature implantation.

Figure 10 shows the simulated normalized damage as a function of temperature for 80 keV C implantation at a dose rate of 5×10^{12} cm^{-2} s^{-1}. For implantation with dynamic annealing, implantations were carried out at various temperatures up to a dose of 1×10^{15} cm^{-2}. Post-annealing of cryogenic temperature implantations were simulated by implanting at −150 °C and subsequently annealing at various temperatures for 10 min after each implantation. All data have been scaled to unity at low temperature (0 °C).

For a dose of 1×10^{15} cm^{-2}, 0 °C is the amorphous-crystalline phase transition temperature of C implanted at 80 keV and 5×10^{12} cm^{-2} s^{-1}, whereby a buried continuous amorphous layer is formed. Implantations at higher temperatures result in damaged Si, but not enough to cause a transition into amorphous phase. Figure 10 shows that the total normalized damage as a result of dynamic annealing is a strong function of temperature between 0 °C and room temperature. Damage decreases with increase in temperature due to the higher rate of dynamic annealing.

As for the cryogenic implants, implantation at −150 °C was done up to a lower dose of 2×10^{14} cm^{-2} to prevent transition into amorphous phase. As a continuous amorphous layer of Si will recrystallize epitaxially at around 550 °C, it would be inappropriate to subject an amorphous layer to subsequent anneals at different temperatures. It can be seen from Fig. 10 that the damage resulting from cryogenic implanta-

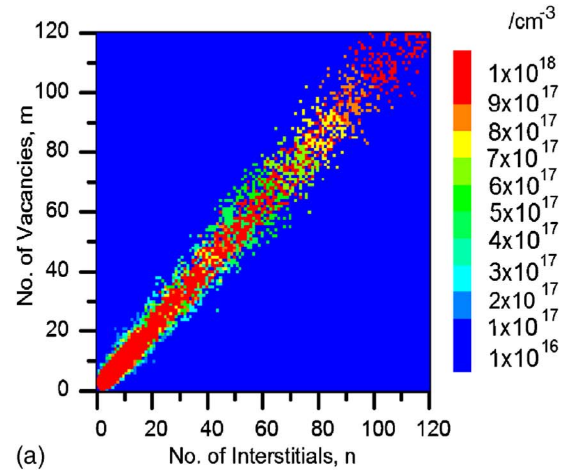

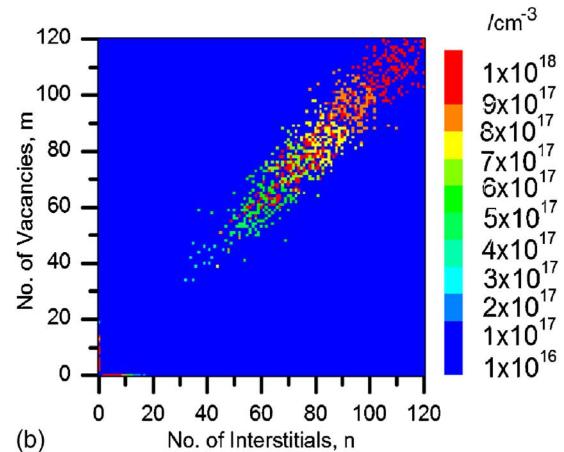

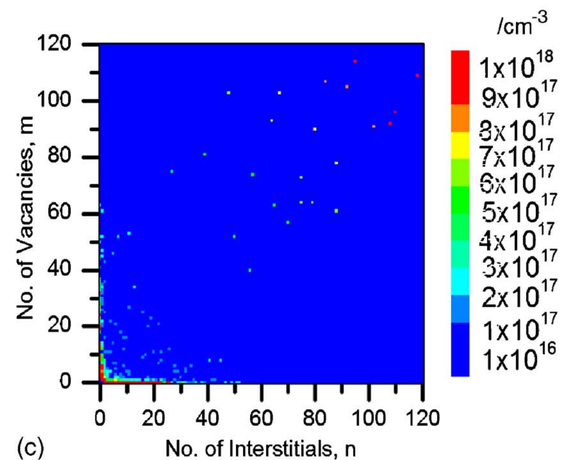

FIG. 11. (Color online) 2D histogram of amorphous pockets composition of (a) cryogenic (−150 °C) C implantation to a dose of 2×10^{14} cm^{-2}, (b) post-cryogenic implantation annealing at 20 °C, and (c) 20 °C C implantation to a dose of 2×10^{14} cm^{-2} (dynamic annealing).

tion is more stable, such that subsequent annealing removes a smaller proportion of the damage than dynamic annealing at the same temperature.

The difference between dynamic annealing and post-implantation annealing of cryogenic implantation is apparent in this model. Figure 11 shows the 2D color map of the amorphous pockets composition under different implantation and annealing conditions. The color represents the concentration of I's and V's in amorphous pockets of a given com-

Downloaded 21 Apr 2008 to 157.88.111.70. Redistribution subject to AIP license or copyright; see http://jap.aip.org/jap/copyright.jsp

position (I, V axes). Figure 11(a) shows the color map of amorphous pockets composition generated by implantation at cryogenic temperature. At this low temperature, amorphous pockets are not recrystallized and are allowed to grow to large sizes. The amorphous pockets generated are well balanced in I and V composition, with a small net balance toward the V axis, indicating a deficit of atoms in the amorphous pockets, in agreement with MD study.[32] Not shown in the color map is the presence of a higher amount of isolated interstitial point defects compared to vacancy point defects, also in agreement with Ref. 32. Figure 11(b) shows the color map of amorphous pocket composition after a subsequent annealing at 20 °C for 10 min. Only the smaller amorphous pockets (with lower activation energy of recrystallization) are annealed, while the larger amorphous pockets remain stable. Figure 11(c) shows that when implantation is carried out at 20 °C, dynamic annealing of the amorphous pockets takes place between successive cascades. Hence, amorphous pockets are not allowed to grow to large sizes. Once an amorphous pocket with a net excess of I's or V's has been completely recrystallized, the local I and V imbalance results in growing population of small, pure $I(I_nV_0)$ and $V(I_0V_m)$ clusters. During implantation, the pure clusters can transform back into an I_nV_m amorphous pockets and have a chance of recrystallizing if a defect of an opposite type is within its capture radius. This allows for a self-consistent treatment of pure clusters and amorphous pockets.

Based on this model, cryogenic temperature implantation allows amorphous pockets to grow to large sizes. Therefore, the damage will be more stable against a given temperature anneal than the damage generated by the same implantation at the same given temperature, in which the amorphous pockets are not allowed to grow as big (and, thereby, as stable) due to dynamic annealing.

IV. CONCLUSIONS

In this work, we have developed a damage accumulation model up to amorphization that is based on the annealing behavior of the amorphous pockets, with the activation energy of recrystallization as a function of the size of the amorphous pockets. This model does not critically depend on the stability of the isolated IV pair, since damage can also nucleate from I_2 and V_2, resulting in more complex amorphous pockets (I_nV_m). Furthermore, it accounts for the contribution of damage from point defects, amorphous pockets, and pure clusters. A number of interesting experimental observations, showing the ion-mass, dose rate, dose, and temperature effects, have been reproduced. In summary, this model has been able to reproduce the ion-mass dependent silicon amorphous-crystalline transition temperature for a wide range of ions, from C to Xe, as a function of dose rate. Thickness of the amorphous layers are well-simulated in a range of amorphizing conditions. In terms of the dose effect, the proportion of amorphous pockets and amorphous damage has been consistently reproduced as a function of dose. In addition, the two-layered damage distribution along the path of a high-energy ion can be simulated, as is consistent with experimental observations. Lastly, this model is able to show that dynamic annealing is more effective at removing damage than post-cryogenic implantation annealing at the same temperature, as amorphous pockets are allowed to grow to larger (and more stable) sizes during cryogenic implantation, than is allowed by dynamic annealing.

[1] E. Chason, S. T. Picraux, J. M. Poate, J. O. Borland, M. I. Current, T. Diaz de la Rubia, D. J. Eaglesham, O. W. Holland, M. E. Law, C. W. Magee *et al.*, J. Appl. Phys. **81**, 6513 (1997).
[2] B. J. Pawlak, R. Surdeanu, B. Colombeau, A. J. Smith, N. E. B. Cowern, R. Lindsay, W. Vandervorst, B. Brijs, O. Richard, and R. Cristiano, Appl. Phys. Lett. **84**, 2055 (2004).
[3] R. D. Goldberg, J. S. Williams, and R. G. Elliman, Nucl. Instrum. Methods Phys. Res. B **106**, 242 (1995).
[4] T. Motooka and O. W. Holland, Appl. Phys. Lett. **61**, 3005 (1992).
[5] O. W. Holland, S. J. Pennycook, and G. L. Albert, Appl. Phys. Lett. **55**, 2503 (1989).
[6] T. Motooka and O. W. Holland, Appl. Phys. Lett. **58**, 2360 (1991).
[7] P. J. Schultz, C. Jagadish, M. C. Ridgway, R. G. Elliman, and J. S. Williams, Phys. Rev. B **44**, 9118 (1991).
[8] R. D. Goldberg, R. G. Elliman, and J. S. Williams, Nucl. Instrum. Methods Phys. Res. B **80-81**, 596 (1993).
[9] L. Pelaz, L. A. Marques, and J. Barbolla, J. Appl. Phys. **96**, 5947 (2004).
[10] R. Karmouch, J.-F. Mercure, Y. Anahory, and F. Schiettekatte, Appl. Phys. Lett. **86**, 031912 (2005).
[11] M. J. Caturla, T. Diaz de la Rubia, L. A. Marques, and G. H. Gilmer, Phys. Rev. B **54**, 16683 (1996).
[12] L. A. Marques, L. Pelaz, M. Aboy, L. Enriquez, and J. Barbolla, Phys. Rev. Lett. **91**, 135504 (2003).
[13] K. R. C. Mok, M. Jaraiz, I. Martin-Bragado, J. E. Rubio, P. Castrillo, R. Pinacho, J. Barbolla, and M. P. Srinivasan, J. Appl. Phys. **98**, 046104 (2005).
[14] M. Jaraiz, P. Castrillo, R. Pinacho, I. Martin-Bragado, and J. Barbolla, in *Simulation of Semiconductor Processes and Devices 2001*, edited by D. Tsoukalas and C. Tsamis (Wien, Austria, Springer, 2001), pp. 10–17.
[15] G. Hobler and G. Otto, Mater. Sci. Semicond. Process. **6**, 1 (2003).
[16] F. F. Morehead, B. L. Crowder, and R. S. Title, J. Appl. Phys. **43**, 1112 (1972).
[17] K. A. Jackson, J. Mater. Res. **3**, 1218 (1988).
[18] L. A. Marques, J. E. Rubio, M. Jaraiz, L. A. Bailon, and J. Barbolla, J. Appl. Phys. **81**, 1488 (1997).
[19] E. C. Baranova, V. M. Gusev, Y. V. Martynenko, C. V. Starinin, and I. B. Haibullin, Radiat. Eff. **18**, 21 (1973).
[20] W. P. Maszara and G. A. Rozgonyi, J. Appl. Phys. **60**, 2310 (1986).
[21] R. Lindsay, B. Pawlak, J. Kittl, K. Henson, C. Torregiani, S. Giangrandi, R. Surdeanu, V. W. A. Mayur, J. Ross *et al.*, in *Material Research Society Proceedings* (MRS, Pittsburgh, 2003), Vol. 765, p. D7.4.
[22] I. Avci, M. E. Law, E. Kuryliw, and K. S. Jones, in *IEDM Technical Digest* (IEDM, Washington, DC, pp. 38.2.1–38.2.4, 2001).
[23] F. Cristiano, N. Cherkashin, P. Calvo, Y. Lamrani, X. Hebras, A. Claverie, W. Lerch, and S. Paul, Mater. Sci. Eng., B **114–115**, 174 (2004).
[24] J. J. Hamilton, E. J. H. Collart, B. Colombeau, C. Jeynes, M. Bersani, D. Giubertoni, J. A. Sharp, N. E. B. Cowern, and K. J. Kirkby, Nucl. Instrum. Methods Phys. Res. B **237**, 107 (2005).
[25] R. Lindsay, R. Severi, B. J. Pawlak, K. Henson, A. Lauwers, X. Pages, A. Satta, R. Surdeanu, H. Lendzian, and K. Maex, in *The Fourth International Workshop on Junction Technology* (IEEE, New York, 2004), pp. 70–75.
[26] B. J. Pawlak, R. Lindsay, R. Surdeanu, P. Stolk, K. Maex, and X. Pages, in *Proceedings of the 14th International Conference on Ion Implantation Technology* (IEEE, New York, 2002), pp. 21–24.
[27] B. Colombeau, F. Cristiano, J.-C. Marrot, G. Ben Assayag, and A. Claverie, Mater. Res. Soc. Symp. Proc. **669**, J481 (2001).
[28] O. W. Holland, L. Xie, B. Nielsen, and D. S. Zhou, J. Electron. Mater. **25**, 99 (1996).
[29] O. W. Holland, M. K. El-Ghor, and C. W. White, Appl. Phys. Lett. **53**, 1282 (1988).
[30] O. W. Holland and C. W. White, Nucl. Instrum. Methods Phys. Res. B **59-60**, 353 (1991).
[31] J. E. Westmoreland, J. W. Mayer, F. H. Eisen, and B. Welch, Appl. Phys. Lett. **15**, 308 (1969).
[32] R. Karmouch, J. F. Mercure, Y. Anahory, and F. Schiettekatte, Appl. Phys. Lett. **86**, 031912 (2005).

Downloaded 21 Apr 2008 to 157.88.111.70. Redistribution subject to AIP license or copyright; see http://jap.aip.org/jap/copyright.jsp